Bulletin of the Seismological Society of America, Vol. 99, No. 1, pp. 352–366, February 2009, doi: 10.1785/0120080058

# Time-Lapse Changes of Seismic Velocity in the Shallow Ground Caused by Strong Ground Motion Shock of the 2000 Western-Tottori Earthquake, Japan, as Revealed from Coda Deconvolution Analysis

by Kaoru Sawazaki, Haruo Sato, Hisashi Nakahara, and Takeshi Nishimura

Abstract A large earthquake shock often drops the seismic velocity of the shallow ground. However, it is not clear whether the dropped velocity recovers shortly after the earthquake shock or not. The purpose of this article is to report the time-lapse changes of seismic velocity in the shallow ground after the 2000 Western-Tottori earthquake, Japan. We deconvolve the coda record of small earthquakes registered on the ground surface by that registered at the 100 m depth in a borehole at a station that experienced a strong shock from the mainshock. Because coda waves are mostly composed of randomly scattered *S* waves, deconvolution of the two coda records enables us to obtain a robust image of the ground structure. Assuming that the shear modulus was reduced at the depth of 0–11 m, we estimate the shear modulus change in each time period after the mainshock by fitting synthetic coda deconvolution to the observed one from 1 to 16 Hz. As a result, the shear modulus dropped to 52% of the value obtained before the mainshock a few minutes after the strong earthquake shock. This caused a decrease in the *S*-wave velocity of 30% and an increase in *S*-wave travel time of 17 msec. The shear modulus continued to recover for over 1 yr following the logarithm of the lapse time. It recovered to 69%, 83%, 87%, and 97% of the value obtained before the mainshock in the periods of 0 to 1 week, 1 week to 1 month, 1 month to 1 yr, and 1 to 4 yr after the mainshock, respectively.

## Introduction

Reduction of seismic velocity in the crust after a large earthquake has been detected by several methods such as artificial explosion sources (Li *et al.*, 1998; Nishimura *et al.*, 2005), repeating earthquake sources (Poupinet *et al.*, 1984; Schaff and Beroza, 2004), and wave interferometry (Pandolfi *et al.*, 2006; Wegler and Sens-Schonfelder, 2007). Some of these studies also reported long-term recovery of the seismic velocity continuing over a few months following the velocity reduction and claimed that the coseismic rupture around the fault zone and/or the volumetric strain change corresponding to the fault motion are responsible for the velocity change. Recently, several studies reported the velocity change in the shallow ground that was damaged by a strong earthquake shock. Rubinstein and Beroza (2004), who measured *S*-wave travel times of repeating earthquakes, detected significant delay in the travel times at the stations that experienced strong ground motion shock by the 1989 Loma-Prieta earthquake. After the mainshock, the travel-time delay continued to recover for a few months. Peng and Ben-Zion (2006) also reported the delay and recovery of the *S* and *S*-coda travel times for the 1999 Düzce earthquake in Turkey. Applying the similar method to the repeating earthquakes located near the fault zone of the 2003 Tokachi-Oki earthquake, Japan, Rubinstein *et al.* (2007) detected the velocity reduction both in the shallow ground and near the rupture zone. The most influential depth for the temporal change in the seismic velocity is still under discussion.

Borehole observation is one of the useful methods to separate the velocity change in the shallow ground from that near the fault zone. Rubinstein and Beroza (2005) who studied the change of the *S*-wave velocity after the 2004 Parkfield earthquake showed that the delays of the *S*-wave travel times of repeating earthquakes are much larger at the sensors located on the ground surface than those at the shallow boreholes. Their study suggests that the region responsible for the large *S*-wave velocity reduction is limited in the shallow ground. Analyzing seismograms registered by borehole array sensors, Pavlenko and Irikura (2002) detected the reduction of the shear modulus at depths less than a few tens of meters at Port Island, Kobe, Japan, during the strong ground motion generated by the 1995 Kobe earthquake. This phenomenon is widely known as a nonlinear site effect caused by a strong earthquake shock, which decreases the shear modulus and increases the attenuation coefficient in the shallow ground

(e.g., Chin and Aki, 1991). Their study provides direct evidence for the velocity reduction in the shallow ground caused by nonlinearity. Sawazaki *et al.* (2006) monitored the spectral ratio of the coda seismograms registered on the ground surface and at a downhole at two sites that experienced strong ground motion shock of the 2000 Western-Tottori earthquake, Japan. Their results showed a clear reduction of the peak frequencies of the coda spectral ratio just after the strong ground motion shock and the following recovery of them continuing for a few years.

Because Sawazaki *et al.* (2006) did not analyze the phase spectrum of the coda spectral ratio, their results cannot be directly related to the velocity change. We overcome this limitation by deconvolving the coda wave record on the ground surface by that at the downhole, where both amplitude and phase spectra are available simultaneously. Because coda waves are considered to be composed of the omnidirectional incoherent *S* waves, the distribution of incident angles is supposed to be statistically uniform for all the earthquakes. Therefore, we can average the coda deconvolutions of many earthquakes in each time period before and after the mainshock to obtain the stable estimates of the velocity change in the shallow subsurface without considering incident angles and source mechanisms of the used earthquakes.

In this article, we apply the coda deconvolution method to data recorded at one KiK-net (Japanese digital strong-motion seismograph network operated by National Research Institute for Earth Science and Disaster Prevention [NIED]) station that is located close to the epicenter of the 2000 Western-Tottori earthquake (6 October 2000, $M_{JMA}$ 7.3). We also theoretically synthesize the coda deconvolution assuming an omnidirectional incidence of random waves to a 1D layered velocity structure. Fitting the theoretical coda deconvolution to the observed one for each time period before and after the mainshock, we estimate the reduction and recovery process of shear modulus in the shallow ground. Then, we evaluate how the *P*- and *S*-wave velocities and corresponding one-way travel times changed after the strong ground motion shock.

## Data

Figure 1 shows the location of station SMNH01 (Hakuta is the Japanese name) of KiK-net (triangle) and epicenters of the earthquakes analyzed (gray circles). The 2000 Western-Tottori earthquake is a strike-slip event (see the focal mechanism) but did not show a clear surface break. Station SMNH01 is located 8 km from the epicenter of the mainshock. The station is equipped with two accelerometers: one is on the ground surface and the other is at the depth of 100 m in a borehole (Okada *et al.*, 2004). The data are sampled every 0.005 sec, and the gain of the recording system is almost flat for frequencies lower than about 20 Hz. Table 1 shows the average lapse time after the mainshock and the number, the magnitude range, and the hypocentral distance range of the used earthquakes for different time periods before and after the mainshock.

Station SMNH01 is located at a mountainous region. According to the well-logging data shown by thick lines in Figure 2, *P*- and *S*-wave travel times from the downhole to

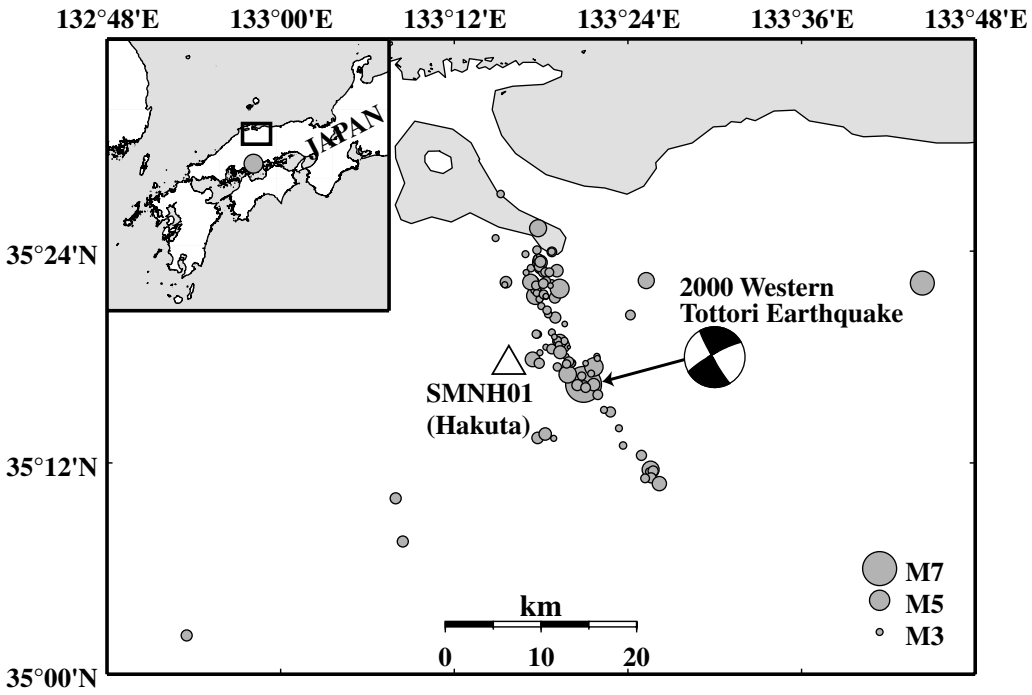


**Figure 1.** Location of the KiK-net SMNH01 station (triangle) and epicenters of the earthquakes used for the analysis (gray circles). The epicenter of the 2000 Western-Tottori earthquake is denoted with a focal sphere.

Table 1
Information for the Used Earthquakes in Each Period

| Period | Average Lapse Time (day) | Number of Earthquakes | $M_{JMA}$ | Hypocentral Distance (km) |
|---|---|---|---|---|
| −2–0 yr | −382 | 3 | 2.9–4.8 | 15–99 |
| 0–10.24 sec (mainshock)* | — | 1 (direct *S*-wave window) | 7.3 | 12 |
| 50–280 sec (mainshock) | 0.002 | 1 (14 coda windows) | 7.3 | 12 |
| 0–1 week | 1.05 | 10 | 3.3–4.7 | 7–16 |
| 1 week to 1 month | 19.4 | 30 | 2.3–4.6 | 7–22 |
| 1 month to 1 yr | 86.4 | 45 | 2.5–4.5 | 7–46 |
| 1–4 yr | 674 | 21 | 2.8–5.5 | 7–46 |

*The data in the period 0–10.24 sec after the mainshock are not used for modeling the velocity structure.

the ground surface are 0.031 and 0.097 sec for the vertical incidence, respectively. Quaternary sandy gravel extends from the ground surface to 13.5 m depth, and Neogene solid basalt extends from 13.5 to 100 m depth. Although the velocity boundary written in the well-logging data (11 m depth) does not correspond to the interface between sandy gravel and basalt (13.5 m depth), we adopt the velocity boundary of the well-logging data throughout the analysis.

Figure 3a and b shows the accelerogram of the earthquake that occurred 84 days before the 2000 Western-Tottori earthquake (we refer to this event as the foreshock) recorded on the ground surface and at the downhole at station SMNH01, respectively. Figure 3c shows the amplitude spectrum of the surface and downhole records as black and gray curves, respectively. The rectangle in each accelerogram indicates the time window used for calculating the amplitude spectrum. Figure 3d, e, and f are the same as Figure 3a, b, and c, respectively, for the data of the mainshock. The maximum acceleration of the mainshock record on the ground surface is 720 cm/sec$^2$ for the north–south component. Although liquefaction was not reported around this station, several studies reported the occurrence of the nonlinear ground responses caused by the strong ground motion shock at this station (e.g., Yamazoe *et al.*, 2004). Here, we use the phrase nonlinear ground response as the breakdown of the linear relationship between the stress and strain (Hooke's law) in the shallow ground by the strong ground motion. On the mainshock, strong accelerations larger than 100 cm/sec$^2$ continued for about 10 sec. In this time period, the amplitude spectral ratio of the surface and downhole records is much different from that observed before the mainshock, which suggests the occurrence of nonlinear response. Because the nonlinearity is considered to be apparent for accelerations larger than about 100–200 cm/sec$^2$ (e.g., Beresnev and Wen, 1996), we think the coda part of the mainshock record with the acceleration less than 100 cm/sec$^2$ may not be strongly affected by the nonlinear effect.

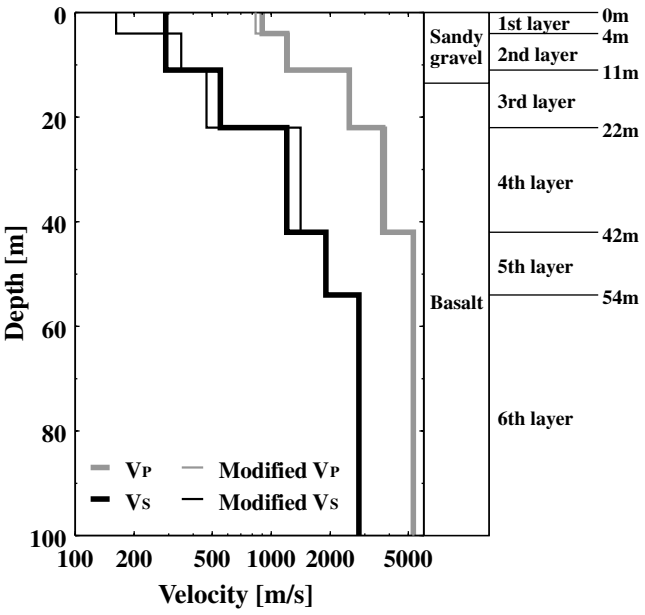


**Figure 2.** *P*- and *S*-wave velocity structures of station SMNH01 with the geologic structure. Thick lines are the *PS* well-logging data from the KiK-net website (see Data and Resources section), and thin lines are the best-fit reference velocity structures estimated by fitting the theoretical coda deconvolution to the observed one obtained before the mainshock. Depths of the layer boundaries are shown in the right-hand side of the figure. Note that the abscissa is the velocity in a logarithmic scale.

## Analysis Procedure of Coda Waves

We first deconvolve a coda record of each earthquake registered on the ground surface by that at the downhole for both the east–west and north–south components. Then, the coda deconvolutions are averaged over plural events that occurred in each time period as shown in Table 1. As we showed in Figure 3c, the amplitude spectrum of the downhole coda record is almost flat. This characteristic of the downhole coda record confirms the stability of the coda deconvolution.

A time window used for calculating the coda deconvolution begins from 2 sec after twice the *S*-wave travel time for each earthquake, where 2 sec is added to avoid the effect of source duration. The length of each coda window is 10.24 sec. The signal-to-noise amplitude ratio of the 1–16 Hz band-pass filtered coda trace is larger than 3 for both records on the ground surface and at the downhole, where the noise records are selected from the pretrigger seismograms before the *P*-wave arrival. The maximum acceleration of the coda

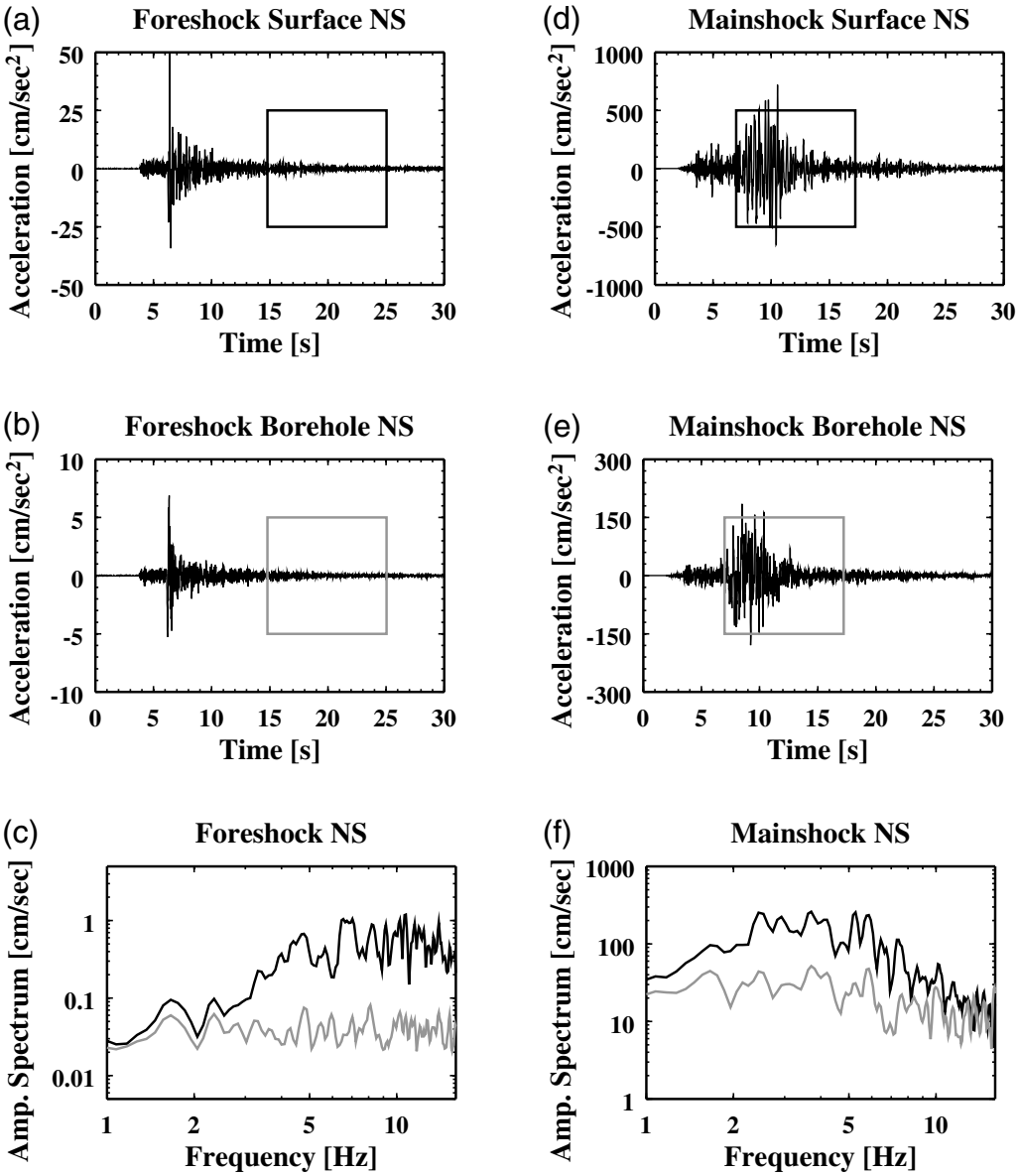


**Figure 3.** North–south component accelerogram of the earthquake that occurred 84 days before the 2000 Western-Tottori earthquake registered (a) on the ground surface and (b) at the downhole at station SMNH01. The abscissa is the lapse time after the origin time. (c) The amplitude spectrum of the surface (black curves) and downhole (gray curves) recorded. The time window used for calculating the amplitude spectrum is indicated by a rectangle in (a) and (b). (d), (e), and (f) are the same as (a), (b), and (c) except that these figures are made for the mainshock record of the 2000 Western-Tottori earthquake.

trace is less than 30 cm/sec$^2$, where the nonlinear response is negligible. We select only the coda windows that satisfy the preceding conditions. For the accelerogram of the mainshock, we select one time window for the direct *S* wave (0–10.24 sec after the *S*-wave arrival) and 14 time windows for coda waves (chosen from 50–280 sec after the *S*-wave arrival, where the signals from large aftershocks are excluded).

After applying a 5% cosine taper to both coda traces on the ground surface and at the downhole, we perform the fast Fourier transform for both traces. Then, we calculate the deconvolution in the frequency domain according to the equation

$$D_i(f) = \frac{S_i(f)}{B_i(f)} = \frac{S_i(f)B_i^*(f)}{|B_i(f)|^2}, \tag{1}$$

where $S_i(f)$ and $B_i(f)$ represent the complex spectra of the coda record for the $i$th earthquake recorded on the ground surface and at the downhole, respectively. $f$ is the frequency in Hz, and the asterisk denotes the complex conjugate. We refer to equation (1) as coda deconvolution throughout this article. Note that equation (1) is not the transfer function to the incident waves because the downhole record may contain not only incident waves but also the waves reflected on the ground surface and/or sediment layer boundaries between

the two sensors. To stabilize the coda deconvolution, we smooth the numerator and denominator of equation (1) by applying a Hanning window one time in the frequency domain (e.g., Soda *et al.* 2001).

We assume that the average of the coda deconvolution represents the real structure of the ground. The average coda deconvolution is given by

$$\bar{D}(f) \equiv \frac{1}{N}\sum_{i=1}^{N} D_i(f), \tag{2}$$

where $N$ is the number of earthquakes used for the averaging in each time period (see Table 1). Amplitude and phase spectra of the average coda deconvolution are given by $|\bar{D}(f)|$ and $\arg[\bar{D}(f)]$, respectively. Using equation (2), we calculate the average of the coda deconvolution for each time period and show its temporal variation.

## Temporal Change in the Observed Coda Deconvolution

Figure 4 shows the amplitude spectrum of the average coda deconvolution obtained in each period (thick curves) and that obtained before the mainshock (thin curves). The dotted vertical line represents the lowest peak frequency observed before the mainshock, which was 4.6 and 4.7 Hz for the east–west and north–south components, respectively. For both components, the amplitude level for frequencies higher than about 4 Hz decreased in the period 0–10.24 sec after the direct *S*-wave arrival of the mainshock. This is a typical nonlinear ground response caused by the strong ground motion, where the increase of attenuation coefficient dropped the amplitude level and the reduction of the shear modulus shifted the peak frequencies to a lower frequency. In the period 50–280 sec after the *S*-wave arrival of the mainshock, the amplitude level almost recovered for both components. However, the peak frequencies were still lower than those observed before the mainshock, although the acceleration was so small that the nonlinearity was negligible in this period. The lowest peak frequency in this period was 4.0 and 3.9 Hz for the east–west and north–south components, respectively, which were 80%–90% of the values obtained before the mainshock. This suggests that the seismic velocity was still lower than the value obtained before the mainshock at this time. After that, the peak frequencies continued to re-

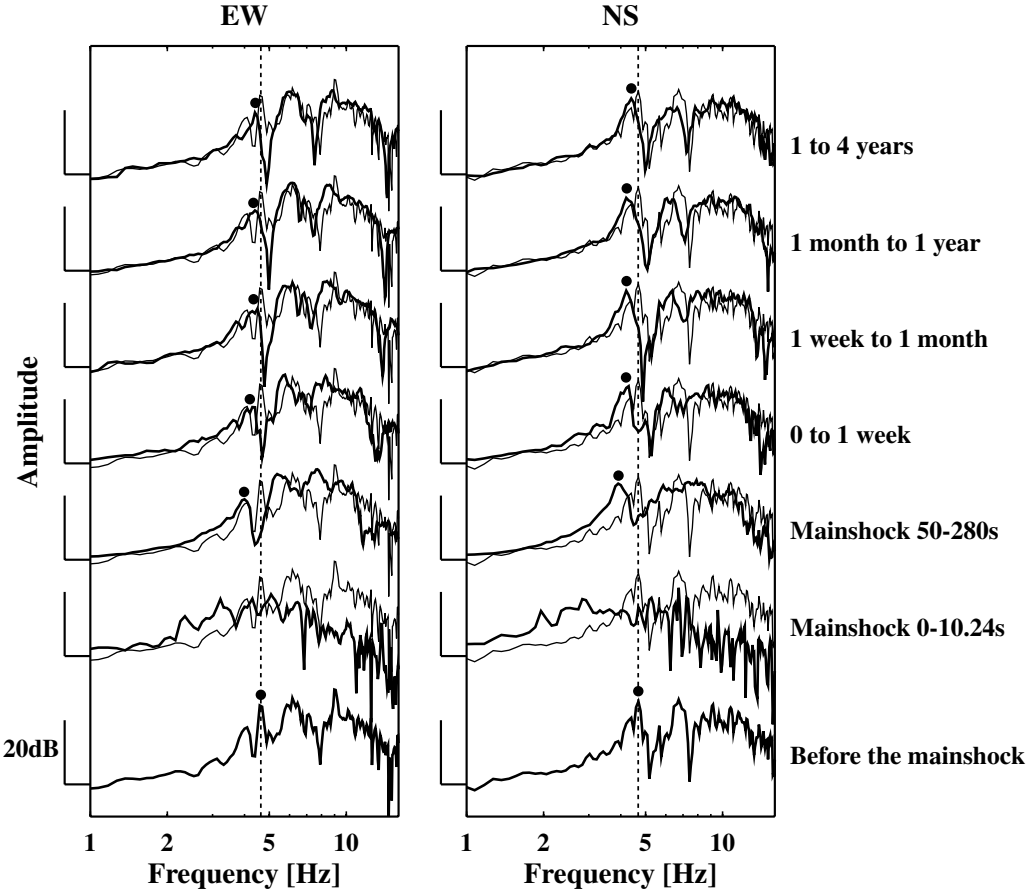


**Figure 4.** Temporal change in the amplitude spectrum of the average coda deconvolution. Thick and thin curves represent the amplitude spectra in each period and those observed before the mainshock, respectively. The amplitude scale is logarithmic and is indicated by a vertical bar in decibels on the left-hand vertical axis. The dotted vertical lines represent the lowest peak frequency observed before the mainshock. The peak frequencies in each period are denoted by black circles.

cover for over 1 yr and approached the values obtained before the mainshock.

The amplitude level of the lowest peak was much lower for the east–west component than that for the north–south component throughout the periods except 0–10.24 sec after the direct *S*-wave arrival of the mainshock. Because we use coda waves for the analysis, the differences between the two components may not be related to variation in back azimuths or polarity of incident waves but may be related to the anisotropic structure in the shallow ground around this station.

Figure 5 shows the phase spectrum of the average coda deconvolution obtained in each period (black circles) and that obtained before the mainshock (open circles). The phase shift increased just after the strong ground motion shock and continued to recover for over 1 yr, approaching the value obtained before the mainshock. Because a larger phase shift means a longer travel time from the downhole to the ground surface, this is direct evidence for the seismic velocity reduction between the ground surface and the downhole sensor.

Figure 6 shows the average coda deconvolution obtained in each period (thick curves) and that obtained before the mainshock (thin curves) in the time domain. The deconvolutions are band-pass filtered from 1 to 16 Hz. The dotted vertical lines represent the peak lag times observed before the mainshock. The coda deconvolutions showed a clear increase of the peak lag time after the mainshock, and the recovery continued over 1 yr. Because the observed peak lag times are almost the same as the one-way *S*-wave travel time calculated from the well-logging data (0.097 sec), a temporal change may reflect a change of the *S*-wave velocity of the ground. The signals of the coda deconvolution appear only on positive lag times. This agrees with the observation by Snieder and Safak (2006), where they deconvolved the record at each floor of a building by the record at the basement.

## Synthesis of the Theoretical Coda Deconvolution

In this section, we explain how to calculate the theoretical coda deconvolution. We assume that incident waves are composed of omnidirectional incoherent *SH* and *SV* waves that are coming from the lower hemisphere with the same amplitude for all the directions (see Fig. 7). Also, the medium from the ground surface to the downhole sensor is assumed to be a 1D stratified structure. We denote the response functions to the horizontal component of the *SH* and *SV* waves as $T_{SH}(\theta, f)$ and $T_{SV}(\theta, f)$ on the ground surface and as $R_{SH}(\theta, f)$ and $R_{SV}(\theta, f)$ at the downhole, respec-

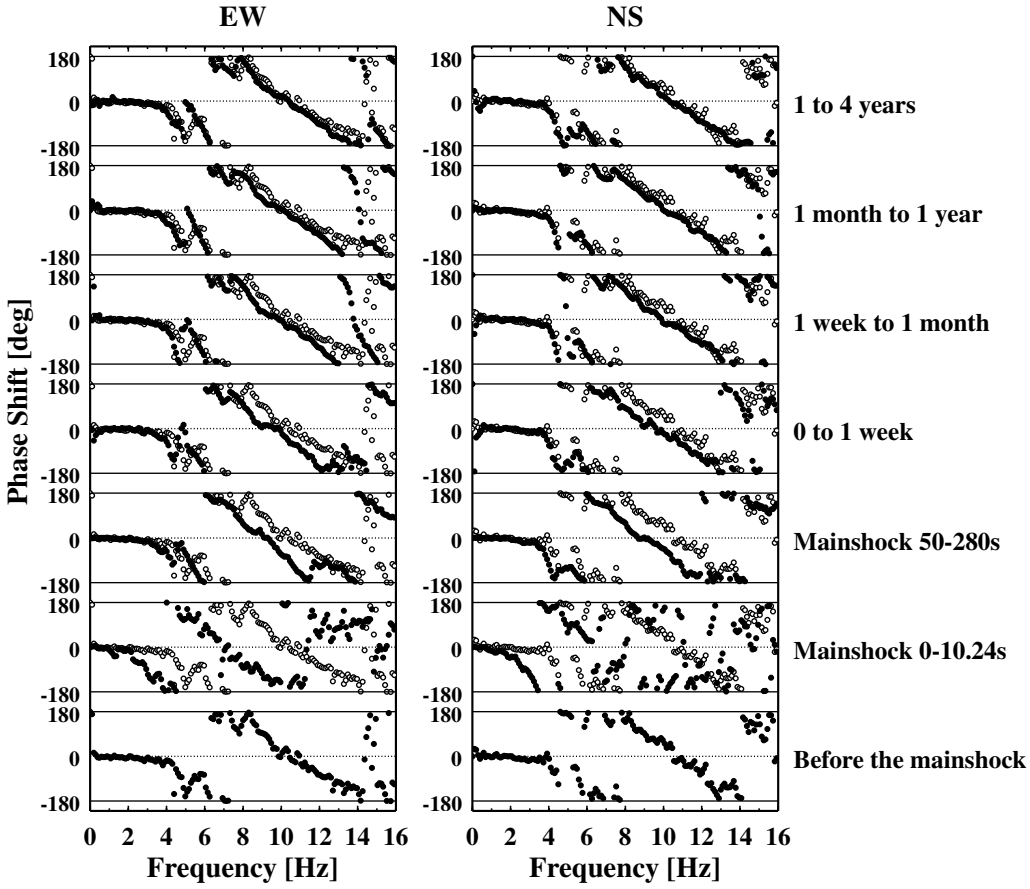


**Figure 5.** Temporal change in the phase spectrum of the average coda deconvolution. Black and open circles represent the phase spectra in each period and those observed before the mainshock, respectively.

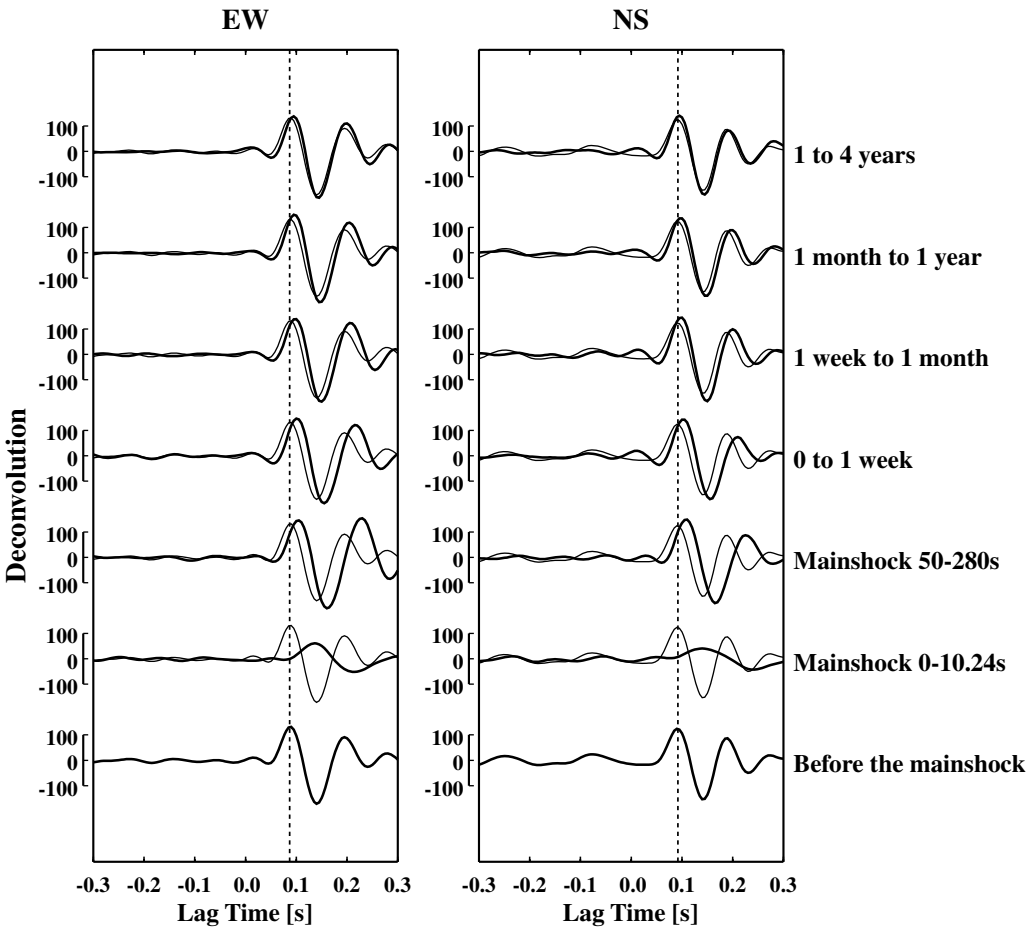


**Figure 6.** Temporal change in the average coda deconvolution in the time domain (1–16 Hz). Thick and thin curves represent the coda deconvolution in each period and that observed before the mainshock, respectively. The dotted vertical lines represent the peak lag time observed before the mainshock.

tively, where $\theta$ is the incident angle. The theoretical coda deconvolution $D^T(f)$ is given by

$$D^T(f) = \frac{\langle S^T(f) B^{T^*}(f) \rangle}{\langle |B^T(f)|^2 \rangle}, \tag{3}$$

where the angular brackets represent the average for the incidence of incoherent waves from any direction (see the appendix). Note that this average is different from the average of the coda deconvolutions for many earthquakes defined by equation (2). The cross and power spectra on the numerator and denominator of equation (3) are given by

$$\begin{aligned} \langle S^T(f) B^{T^*}(f) \rangle &= \pi |A(f)|^2 \int_0^{\pi/2} [T_{SH}(\theta, f) R^*_{SH}(\theta, f) \\ &\quad + T_{SV}(\theta, f) R^*_{SV}(\theta, f) \cos^2\theta] \sin\theta \, d\theta, \\ \langle |B^T(f)|^2 \rangle &= \pi |A(f)|^2 \int_0^{\pi/2} [|R_{SH}(\theta, f)|^2 \\ &\quad + |R_{SV}(\theta, f)|^2 \cos^2\theta] \sin\theta \, d\theta. \end{aligned} \tag{4}$$

The derivation of equation (4) is shown in the appendix. $|A(f)|^2$ is the average power spectrum of the incident $SH$ and $SV$ waves (see equation A9 in the appendix), which is cancelled by calculating equation (3). We calculate the response functions $T_{SH}(\theta, f)$, $T_{SV}(\theta, f)$, $R_{SH}(\theta, f)$, and $R_{SV}(\theta, f)$ using the modified propagator matrix method by Silva (1976). Instead of integrating over $\theta$ in equation (4), we numerically sum the integrands for $\theta$ from 5° to 85° by 10° intervals.

## Estimation of the Shear Modulus Change

Fitting the theoretical coda deconvolution calculated by equation (3) to the observed one, we estimate the best-fit shear modulus structure in each period. Considering the lithology of the ground at station SMNH01, we assume that the reduction of the shear modulus occurred only in the 0–11 m depths because the medium property is easily changed by strong ground motion especially in cohesionless soil. We search the percentage of the shear modulus reduction at the 0–11 m depths for each period after the mainshock. Because the amplitude spectra of the east–west and north–south components are different (see Fig. 4), we cannot fit the theoretical coda deconvolution to both components simultaneously by the same velocity structure. Therefore, we fit the theoreti-

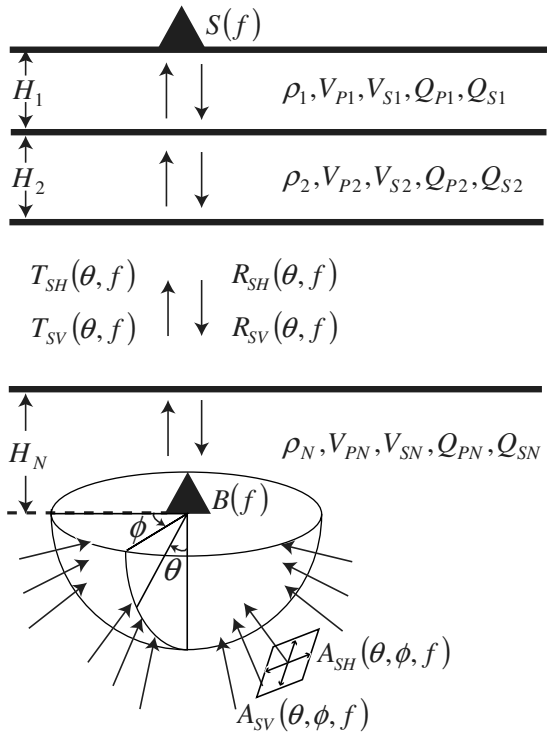


**Figure 7.** Schematic illustration of coda wave propagation in a laterally stratified medium. $A_{SV}(\theta,\phi,f)$ and $A_{SH}(\theta,\phi,f)$ are the spectra of the incident *SV* and *SH* waves, respectively, with incident angle $\theta$ and back azimuth $\phi$. Response functions to horizontal components of the incident wave $A_{SV}(\theta,\phi,f)$ and $A_{SH}(\theta,\phi,f)$ are denoted by $T_{SV}(\theta,f)$ and $T_{SH}(\theta,f)$ on the ground surface and by $R_{SV}(\theta,f)$ and $R_{SH}(\theta,f)$ at the downhole, respectively. $\rho$, $V_P$, $V_S$, $Q_P$, $Q_S$ are density, *P*- and *S*-wave velocities, and attenuation factors for the *P* and *S* waves of each layer, respectively.

cal coda deconvolution only to the north–south component because the lowest peaks are clearly observed for the north–south component compared to those for the east–west component. Also, we do not use the record of 0–10.24 sec after the *S*-wave arrival of the mainshock for the fitting because the nonlinear behavior of the ground cannot be dealt with by the propagator matrix method.

According to the well-logging data, the medium from the ground surface to the downhole is divided into six layers (see Fig. 2). The bottom layer is assumed to extend infinitely below the 100 m depth. Using *P*- and *S*-wave velocity ($V_P$ and $V_S$ in meters per second, respectively) structures and the empirical relationship between $V_P$ and density $\rho$ (in kilograms per cubic meter),

$$\rho = 310 V_P^{0.25} \tag{5}$$

by Gardner *et al.* (1974), we calculate the bulk and shear modulus structures. We also suppose that $Q_P$ and $Q_S$ are given by

$$Q_P = Q_S = Q_0 f^{0.52}, \tag{6}$$

where the frequency dependence $f^{0.52}$ is adopted from the analysis result by Fukushima *et al.* (1992), who measured $Q_S$ of the Pliocene mudstone at depths shallower than 732 m from the borehole observation in Kanto, Japan. Although they estimated the $Q_0$ value as 19, we do not adopt this value in our analysis. For simplicity, we assume that $Q_0$ does not vary with layers.

To estimate the reduction percentage of the shear modulus, it is necessary to make a reference structure that fits to the coda deconvolution observed before the mainshock. At first, we calculated the synthetic coda deconvolution using the well-logging data; however, the synthesis did not fit the observation. Therefore, we modify the well-logging data so that the synthetic coda deconvolution fits well to the observed one obtained before the mainshock. The modification is carried out for the shear modulus of the upper four layers (the 0–42 m depths) and $Q_0$ by a genetic algorithm (GA). The shear modulus is searched within 16% and 144% of the values calculated from the well-logging data, and $Q_0$ is searched within 0.5 and 20. The misfit function is defined as

$$\text{misfit} \equiv \sum_{f=1\text{ Hz}}^{16\text{ Hz}} |\bar{D}(f) - D^T(f)|^2. \tag{7}$$

Because both $\bar{D}(f)$ and $D^T(f)$ are complex functions, the fitting is carried out for both the amplitude and phase spectrum of the coda deconvolution. The shear modulus of the lower two layers (the 42–100 m depths), the bulk modulus, and the densities are fixed to the values calculated from the well-logging data. We run the GA five times with different starting seeds and select the best-fit model among them. We show the best-fit reference velocity structure with thin lines in Figure 2. The $Q_0$-value is estimated as 3.04. We note that the variation of the velocity structures estimated from the five runs of the GA is within 2.6% for all the layers. The $Q_0$-value estimated from the five runs varies from 2.95 to 3.36.

Next, we search the reduction percentage of the shear modulus of the 0–11 m depths by the grid search method for five time periods after the mainshock. The percentage of the shear modulus reduction is the same for both 0–4 m and 4–11 m depth layers and is searched within 20% and 100% of the reference values. The shear modulus of the 11–100 m depths and other parameters such as $Q_0$, bulk modulus, and density are fixed to the values of the reference structure.

## Temporal Change in the Shear Modulus, Seismic Velocity, and One-Way Travel Times

We show the comparison of the observations and the best-fit syntheses in Figure 8, where Figure 8a and b is the amplitude and phase spectra of the average coda deconvolution, respectively and Figure 8c is the average coda deconvolution in the time domain. The observations and syntheses are shown by black and gray curves in Figure 8a and c and by black and gray circles in Figure 8b, respectively. Although Figure 8a is shown in a logarithmic scale, the fitting is carried out by linear frequency intervals. The lowest peak frequency of the theoretical amplitude spectra fits the

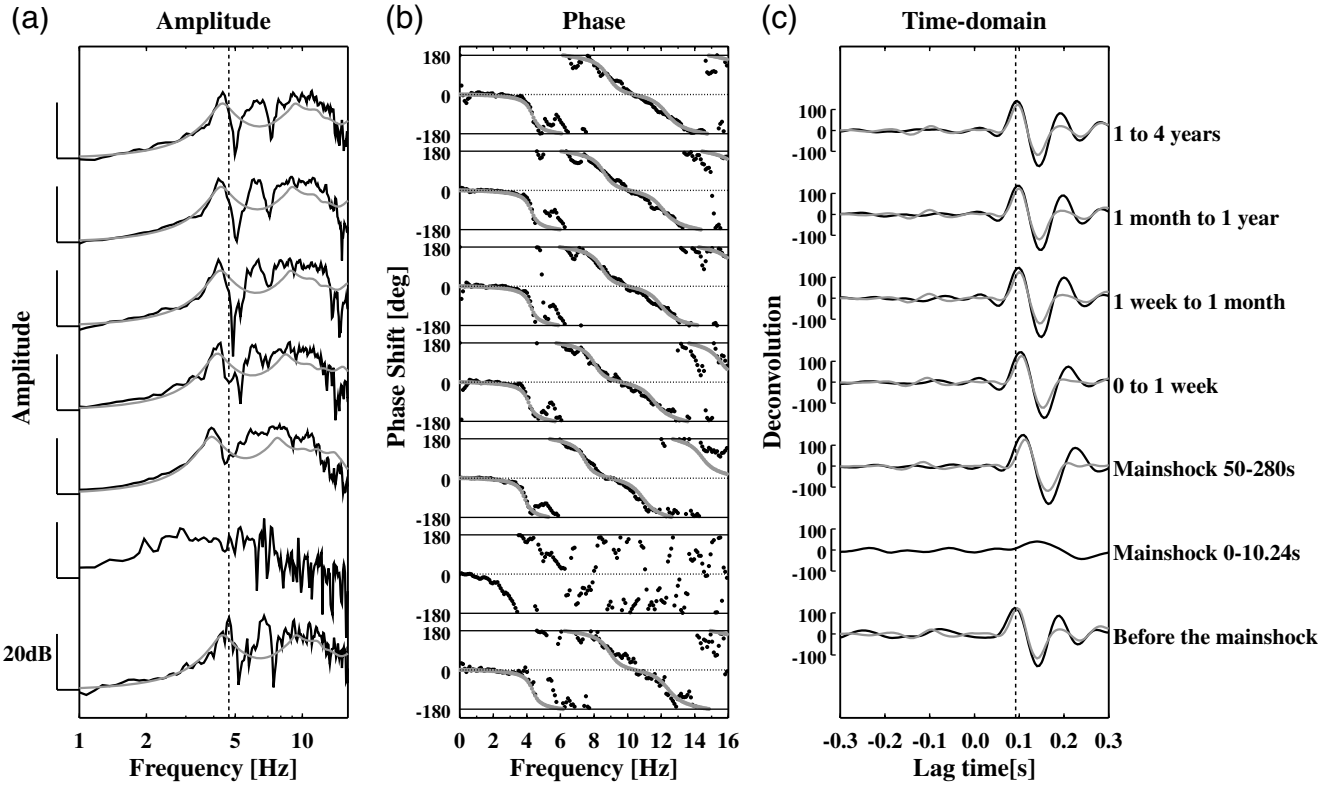


**Figure 8.** Comparison of the best-fit syntheses and the observations for (a) amplitude spectra, (b) phase spectra, and (c) time-domain waveforms of the average coda deconvolution for the north–south component. Observations and syntheses are denoted by black and gray curves for (a) and (c) and by black and gray circles for (b), respectively.

observations well. However, the fit is not good in frequencies higher than the lowest peak frequencies. Especially, strong notches around 5 and 15 Hz are not fitted well. The theoretical phase spectra fit the observations well in frequencies from 1 to 16 Hz except around 5 and 15 Hz, where the observed phase spectra are fluctuating. The theoretical time-domain deconvolutions fit the observations well except for the amplitude of the later phases. The modeling of 1D stratified layers has a limitation if the real ground structure includes 3D heterogeneity. We confirmed that the coherence between the surface and downhole records is relatively low around 5 and 15 Hz, which implies the existence of the strong scattering by 3D heterogeneity at these frequencies. We think the misfit around 5 and 15 Hz may be related to the 3D heterogeneity of the real ground structure that cannot be modeled.

We show the estimated temporal change in shear modulus in Figure 9a. The abscissa is the lapse time measured from the *S*-wave arrival time of the mainshock in a logarithmic scale, and the ordinate is the shear modulus normalized by the value obtained before the mainshock in a linear scale. In the period of 50–280 sec (0.002 day) after the *S*-wave arrival of the mainshock, the shear modulus at the 0–11 m depth dropped to 52% of the value obtained before the mainshock. It continued to recover for over 1 yr following the logarithm of the lapse time. The shear modulus recovered to 69%, 83%, 87%, and 97% of the value obtained before the mainshock in the periods of 0 to 1-week, 1-week to 1-month, 1-month to 1-yr, and 1 to 4 yr after the mainshock, respectively.

Temporal changes in *P*- and *S*-wave velocity structures are shown in Figure 9b and c, where the gray symbols are the values fixed to those obtained before the mainshock throughout the periods. *P*-wave velocity dropped only by a few percent in the period 50–280 sec after the *S*-wave arrival of the mainshock. Because the $V_P/V_S$ ratio in the period before the mainshock is 5.1 for the 0–4 m depth and 3.5 for the 4–11 m depth, both of which are much larger than 1.73 for the Poisson medium, the bulk modulus is much larger than the shear modulus at these depth ranges. Because the bulk modulus is fixed throughout the analysis, change of the shear modulus does not cause drastic change in the *P*-wave velocity. However, the *S*-wave velocity, which is proportional to the square root of the shear modulus, dropped by 30% after the mainshock and continued to recover for over 1 yr.

Using *P*- and *S*-wave velocity structures estimated for each time period, we calculate the temporal change in the one-way travel times of *P* and *S* waves for the vertical incidence. We show the results in Figure 9d and e. In the period 50–280 sec after the *S*-wave arrival of the mainshock, the one-way *S*-wave travel time increased by 17 msec. On the other hand, the increase of the one-way *P*-wave travel time was only 0.4 msec.

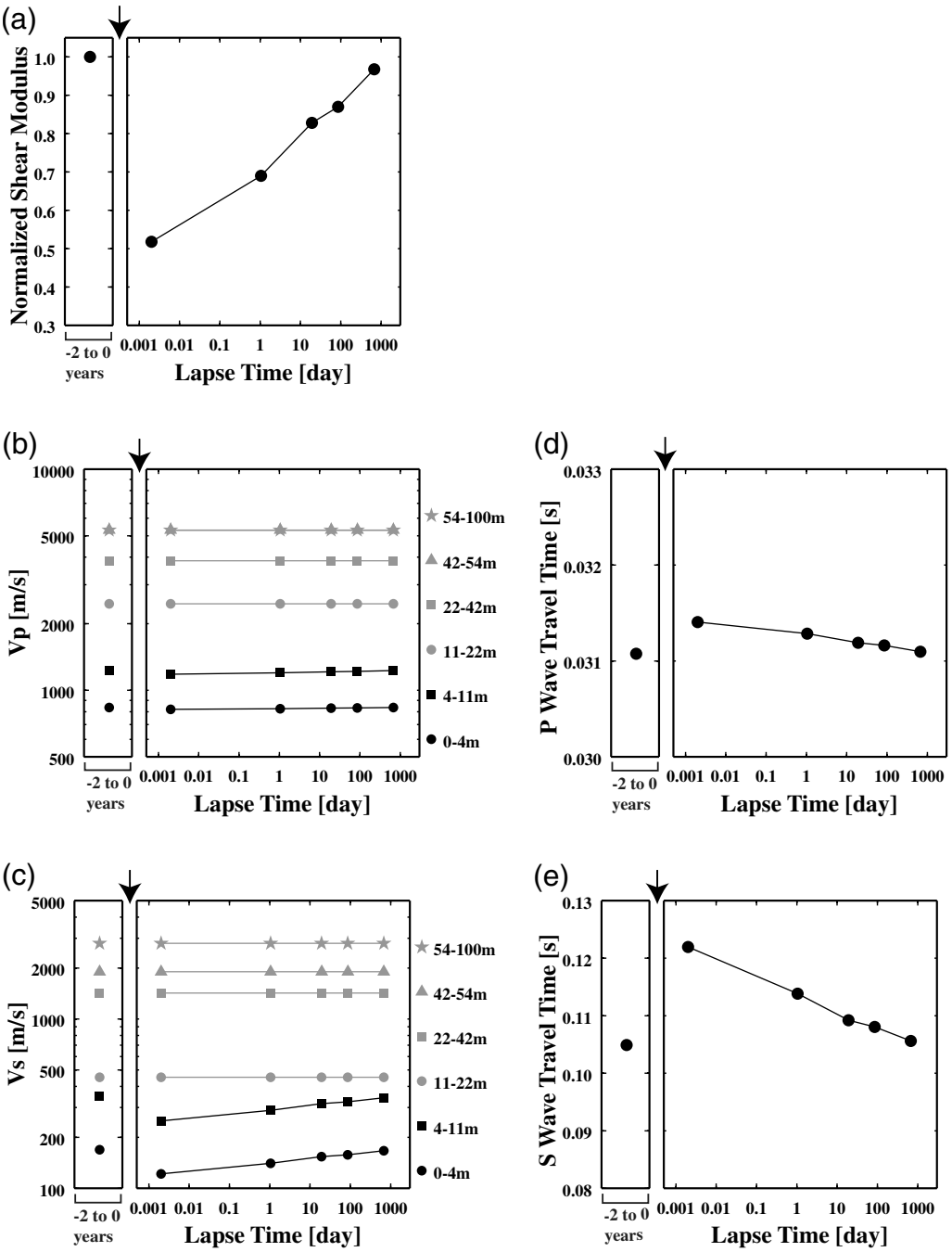


**Figure 9.** Temporal change in (a) the shear modulus at 0–11 m depth normalized by the value obtained before the mainshock, (b) the *P*-wave velocity structure, (c) the *S*-wave velocity structure, (d) the one-way *P*-wave travel time, and (e) the one-way *S*-wave travel time. All figures are made for the north–south component. The left-hand panel of each figure shows the values obtained before the mainshock (the reference model). The right-hand panel shows the temporal change in each value after the mainshock, where abscissa is the lapse time after the *S*-wave arrival of the mainshock in a logarithmic scale. We use the average lapse time in each time period written in Table 1 for plotting. Arrows represent the mainshock occurrence.

## Application of the Cross-Correlation Function Analysis

Recently, many researchers who study on seismic interferometry use a cross-correlation function of two coda or ambient noise records to measure the average seismic velocity between the two separated points (e.g., Campillo and Paul, 2003). In this section, we apply the conventional cross-correlation function method to the surface and the downhole seismograms of SMNH01 and compare the results to the velocity structure estimated from the coda deconvolution method.

Figure 10 shows the north–south component of the cross-correlation function of coda records averaged for the

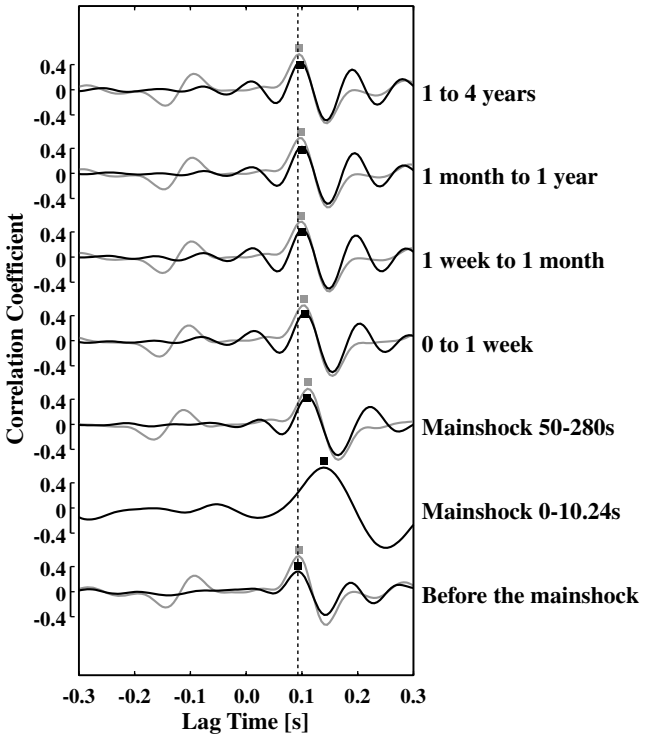


**Figure 10.** Temporal change in the cross–correlation function of coda waves (1–16 Hz) for the north–south component. Black and gray curves represent the observed and synthetic cross–correlation functions, respectively. The correlation coefficient is indicated on the left-hand side of the figure. The dotted vertical line represents the peak lag time of the cross-correlation function observed before the mainshock (0.093 sec). The observed and theoretical peak lag times are denoted by black and gray squares, respectively.

earthquakes that occurred in each period. The black and gray curves represent the observations and syntheses calculated from the estimated structures shown in Figure 9b and c, respectively. The cross-correlation functions are calculated after applying the band-pass filter from 1 to 16 Hz to both the surface and downhole records and are normalized by the square root of integrated power of the two records. The peak lag times plotted by black and gray squares in Figure 10 are calculated by fitting the quadratic function to the peak of the cross-correlation functions. The dotted vertical line indicates the observed peak lag time obtained before the mainshock.

The observed cross-correlation functions show clear peaks only on positive lag times, which means that the downgoing waves reflected on the ground surface are much weaker than the upgoing waves in coda record. On the other hand, the syntheses show peaks on both positive and negative lag times, where the peaks on the negative lag time are smaller than those on the positive lag time because intrinsic attenuation weakens the amplitude of the reflected waves. To eliminate the peaks on the negative lag time, the $Q_0$-value must be less than about one-third of the estimated value. However, in such a small $Q_0$-value, the theoretical amplitude spectrum does not generate steep peaks that are shown in the observed amplitude spectrum (see Fig. 8a). Therefore, the disappearance of the downgoing waves in the observed cross-correlation function cannot be explained by only intrinsic attenuation. We think strong scattering due to the 3D heterogeneity of the shallow ground and/or complex topography around the station SMNH01 may affect the disappearance of the downgoing waves in this case. We note that many studies on borehole observation of the direct *S* waves detected clear downgoing waves (e.g., Kinoshita and Ohike, 2006; Mehta *et al.*, 2007).

The peak lag time of the cross–correlation function increased in the period 0–10.24 sec after the direct *S*-wave arrival of the mainshock because the *S*-wave velocity dropped due to the nonlinear response. In the period 50–280 sec after the *S*-wave arrival, the peak lag time was 0.110 sec, which was still 17 msec longer than the value obtained before the mainshock. After that, the peak lag time continued to recover for over 1 yr and approached the value obtained before the mainshock.

Figure 11 shows the temporal change in the one-way *S*-wave travel time estimated from the coda deconvolution method (black circles; same as in Fig. 9e) and that in the peak lag times of the observed and synthetic cross-correlation functions (black and gray squares, respectively). The peak lag times of the synthetic cross-correlation functions are almost coincident to those of the observations, which confirms that the velocity models estimated from the coda deconvolution method properly explains the peak lag times of the ob-

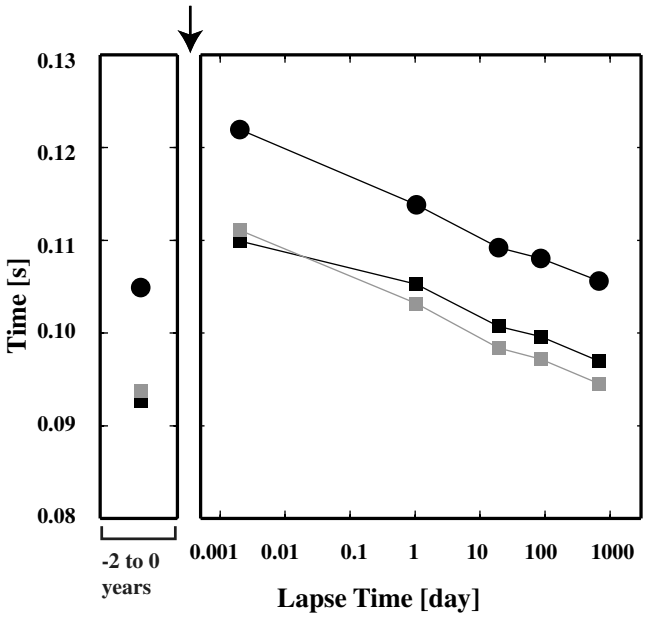


**Figure 11.** Comparison of the one-way *S*-wave travel times calculated from the best-fit *S*-wave velocity structure (black circles, same as Fig. 9e) and the peak lag times of the observed (black squares) and theoretical (gray squares) cross–correlation functions for the north–south component. The left-hand and right-right panels are the same as in Fig. 9. The arrow represents the mainshock occurrence.

served cross-correlation functions. The absolute value of the peak lag times is shorter than that of the one-way *S*-wave travel time by nearly 0.01 sec for all the periods. This is because the travel time of the inclined incident wave is shorter than that of the vertical incident wave: one-way *S*-wave travel time is calculated for the vertical incident waves, whereas the peak lag time of the cross-correlation function of coda waves represents the travel times of the omnidirectional waves, where inclined incident waves are included.

## Possible Mechanisms of the Temporal Change in Shear Modulus

Shear modulus reduction at station SMNH01 during the strong ground motion of the 2000 Western-Tottori earthquake was estimated by Pavlenko and Irikura (2006). According to their results, the shear modulus dropped by 60% from the value of the infinitesimal strain level at the 0–12 m depths during the strong ground motion shock. Because our estimation for the shear modulus reduction is about 50% at the 0–11 m depths in the period of 50–280 sec after the *S*-wave arrival of the mainshock, the two results are almost consistent. We are convinced that the strong ground motion shock caused the shear modulus reduction in the shallow ground.

One of the possible mechanisms for the drop and recovery of the shear modulus in the shallow ground is the change of the fluid system. Once a strong ground motion shock increases pore pressure in the shallow ground, it causes a drop of the frictional strength between soil grains (e.g., Ishihara, 1996). For the recovery process, permeability of soil is a critical parameter. If the drainage of water takes a long time after the strong ground motion shock, the recovery of the shear modulus also takes a long time. For example, Pavlenko and Irikura (2002) detected the depth dependence of the recovery of the ground shear modulus continued for more than a few minutes at Port Island, Japan, after the 1995 Kobe earthquake. Their observation suggests the movement of groundwater after the large earthquake. Snieder and van den Beukel (2004) numerically showed how drainage affects the shear modulus change. To confirm the relationship between the recovery process in the shallow ground and the water drainage effect, it is necessary to record the water pressure and strong ground motion at borehole arrays simultaneously.

Although we assumed that the 0–11 m depths are responsible for the shear modulus reduction, we do not deny the possibility of a shear modulus reduction in the layers deeper than 11 m. Because the lithology of station SMNH01 is solid basalt at depths deeper than 13.5 m, fractures can be generated by the strong ground motion at this depth. It is known that the time dependence of frictional strength between two rocks is proportional to the logarithm of the lapse time after the contact of the rocks (e.g., Dieterich, 1978). Many studies observed the log-linear recovery of seismic velocity near the shallow ground (e.g., Schaff and Beroza, 2004), which was considered to be the healing process of fractures after a large earthquake. The rock experiment by TenCate *et al.* (2000) also showed the log-linear recovery of the resonance frequency of rock samples (on the order of kilohertz) that continues over 1000 sec after large strain oscillation. Thus, the log-linear recovery of the shear modulus is widely observed. We think the log-linear recovery observed in our study can also be related to the healing mechanism of the frictional strength between rocks or soil grains.

The drop and recovery process of the shear modulus depends on the properties of soils such as permeability, fluid content, and so on. Also, they depend on the intensity of the ground motion. This information is necessary for further study of the temporal change in the shallow ground. Other KiK-net data that have experienced strong ground motions are available to study these relationships. Borehole arrays equipped with multiple sensors are also useful to constrain the depth dependence of the drop and recovery process.

## Conclusion

For the precise estimation of the velocity structure in the shallow ground, we develop a method to calculate the deconvolution of two coda records utilizing the random omnidirectional property of coda waves. Applying the coda deconvolution method to the vertical pair of accelerograms, we detect the temporal change in both the amplitude and phase spectra of the average coda deconvolution at the station that experienced the strong ground motion shock from the 2000 Western-Tottori earthquake, Japan. These spectra showed the recovery continuing over 1 yr. On the other hand, the peak level of the amplitude spectrum recovered within a few minutes after the strong ground motion shock. Assuming that the structure shallower than 11 m was responsible for these temporal changes, we estimate the shear modulus reduction in each time period. The shear modulus dropped to 52% of the value obtained before the mainshock in the period 50–280 sec after the *S*-wave arrival of the mainshock. The shear modulus reduction caused a decrease of the *S*-wave velocity of 30% and an increase of the one-way *S*-wave travel time of 17 msec. The recovery of the shear modulus continued over 1 yr following the logarithm of the lapse time after the mainshock. The shear modulus recovered to 69%, 83%, 87%, and 97% of the value obtained before the mainshock in the periods of 0 to 1-week, 1-week to 1-month, 1-month to 1-yr, and 1 to 4 yr after the mainshock, respectively. We checked that these results obtained from the coda deconvolution method are consistent with the results obtained from the conventional cross-correlation function method.

The mechanism of long-term recovery observed in the shallow ground may be related to water drainage and/or fractures generated in the solid rock. To reveal the recovery mechanism, it is necessary to analyze the data recorded by many borehole sensors that experienced strong ground

motions. Especially, strong ground motion data which are simultaneously observed with water pressure will be helpful to understand the relationship between the recovery mechanism and the water drainage effects.

## Data and Resources

KiK-net strong-motion record and *PS* well-logging data are available from the KiK-net website: http://www.kik.bosai.go.jp/kik/index_en.shtml (last accessed November 2008). All figures were produced using the Generic Mapping Tools (GMT; http://gmt.soest.hawaii.edu, last accessed November 2008).

## Acknowledgments

We are grateful to Shin Aoi and Hiroyuki Fujiwara for helpful suggestions and comments about the use of borehole data. We are also grateful to Shigeo Kinoshita for his helpful discussions and comments. We thank the NIED for providing us with the strong-motion records of KiK-net. We also thank Roel Snieder and an anonymous reviewer for their helpful suggestions and comments to improve our article. Kaoru Sawazaki is grateful for support from the Japan Society for the Promotion of Science (JSPS) and the twenty-first century Center of Excellence (COE) program *Advanced Science and Technology Center for the Dynamic Earth* at Tohoku University.

## References

Beresnev, I. A., and K. L. Wen (1996). Nonlinear soil response—a reality?, *Bull. Seismol. Soc. Am.* **86,** 1964–1978.

Campillo, M., and A. Paul (2003). Long-range correlations in the diffuse seismic coda, *Science* **299,** 547–549.

Chin, B. H., and K. Aki (1991). Simultaneous study of the source, path, and site effects on strong ground motion during the 1989 Loma Prieta earthquake: a preliminary result on pervasive nonlinear site effects, *Bull. Seismol. Soc. Am.* **81,** 1859–1884.

Dieterich, J. H. (1978). Time-dependent friction and the mechanics of the stick-slip, *Pure Appl. Geophys.* **116,** 790–806.

Fukushima, Y., S. Kinoshita, and H. Sato (1992). Measurement of $Q-1$ for *S* waves in mudstone at Chikura, Japan: comparison of incident and reflected phases in borehole seismograms, *Bull. Seismol. Soc. Am.* **82,** 148–163.

Gardner, G. H. F., L. W. Gardner, and A. R. Gregory (1974). Formation velocity and density—the diagnostic basics for stratigraphic traps, *Geophysics* **39,** 770–780.

Ishihara, K. (1996). *Soil Behavior in Earthquake Geotechnics*, Oxford Univ. Press, New York, 360 pp.

Kinoshita, S., and M. Ohike (2006). Coherency characteristics of body waves traveling in a sedimentary layer-basement system in the Kanto region, Japan, *Bull. Seismol. Soc. Am.* **96,** 165–175.

Li, Y. G., J. E. Vidale, K. Aki, F. Xu, and T. Burdette (1998). Evidence of shallow fault zone strengthening after the 1992 *M*7.5 Landers, California, earthquake, *Science* **279,** 217–219.

Mehta, K., R. Snieder, and V. Graizer (2007). Extraction of near-surface properties for a lossy layered medium using the propagator matrix, *Geophys. J. Int.* **169,** 271–280.

Nishimura, T., S. Tanaka, T. Yamawaki, H. Yamamoto, T. Sano, M. Sato, H. Nakahara, N. Uchida, S. Hori, and H. Sato (2005). Temporal changes in seismic velocity of the crust around Iwate volcano, Japan, as inferred from analyses of repeated active seismic experiment data from 1998 to 2003, *Earth Planets Space* **57,** 491–505.

Okada, Y., K. Kasahara, S. Hori, K. Obara, S. Sekiguchi, H. Fujiwara, and A. Yamamoto (2004). Recent progress of seismic observation networks in Japan—Hi-net, F-net, K-net and KiK-net, *Earth Planet. Space* **56,** 15–28.

Pandolfi, D., C. J. Bean, and G. Saccorotti (2006). Coda wave interferometric detection of seismic velocity changes associated with the 1999 $M = 3.6$ event at Mt. Vesuvius, *Geophys. Res. Lett.* **33,** L06306, doi 10.1029/2005GL025355.

Pavlenko, O. V., and K. Irikura (2002). Changes in shear moduli of liquefied and nonliquefied soils during the 1995 Kobe earthquake and its aftershocks at three vertical-array sites, *Bull. Seismol. Soc. Am.* **92,** 1952–1969.

Pavlenko, O. V., and K. Irikura (2006). Nonlinear behavior of soils revealed from the records of the 2000 Tottori, Japan, earthquake at stations of the digital strong-motion network, *Bull. Seismol. Soc. Am.* **96,** 2131–2145.

Peng, Z., and Y. Ben-Zion (2006). Temporal changes of shallow seismic velocity around the Karadere-Duzce branch of the North Anatolian fault and strong ground motion, *Pure Appl. Geophys.* **163,** 567–600.

Poupinet, G., W. L. Ellsworth, and J. Frechet (1984). Monitoring velocity variations in the crust using earthquake doublets: an application to the Calaveras fault, California, *J. Geophys. Res.* **89,** 5719–5731.

Rubinstein, J. L., and G. C. Beroza (2004). Evidence for widespread nonlinear strong ground motion in the $M_w$ 6.9 Loma Prieta earthquake, *Bull. Seismol. Soc. Am.* **94,** 1595–1608.

Rubinstein, J. L., and G. C. Beroza (2005). Depth constraints on nonlinear strong ground motion from the 2004 Parkfield earthquake, *Geophys. Res. Lett.* **32,** L14313, doi 10.1029/2005GL023189.

Rubinstein, J. L., N. Uchida, and G. C. Beroza (2007). Seismic velocity reductions caused by the 2003 Tokachi-Oki earthquake, *J. Geophys. Res.* **112,** B05315, doi 10.1029/2006JB004440.

Sawazaki, K., H. Sato, H. Nakahara, and T. Nishimura (2006). Temporal change in site response caused by earthquake strong motion as revealed from coda spectral ratio measurement, *Geophys. Res. Lett.* **33,** L21303, doi 10.1029/2006GL027938.

Schaff, D. P., and G. C. Beroza (2004). Coseismic and postseismic velocity changes measured by repeating earthquakes, *J. Geophys. Res.* **109,** B10302, doi 10.1029/2004JB003011.

Silva, B. W. (1976). Body waves in a layered anelastic solid, *Bull. Seismol. Soc. Am.* **66,** 1539–1554.

Snieder, R. (2004). *A Guided Tour of Mathematical Methods for the Physical Sciences*, Second Ed., Cambridge Univ. Press, Cambridge, 507 pp.

Snieder, R., and E. Safak (2006). Extracting the building response using seismic interferometry: theory and application to the Millikan Library in Pasadena, California, *Bull. Seismol. Soc. Am.* **96,** 586–598.

Snieder, R., and A. van den Beukel (2004). The liquefaction cycle and the role of drainage in liquefaction, *Granul. Matter* **6,** 1–9.

Soda, Y., T. Matsuzawa, and A. Hasegawa (2001). Seismic velocity structure of the crust and uppermost mantle beneath the northeastern Japan arc estimated from receiver functions (in Japanese with English abstract), *J. Seismol. Soc. Jpn.* **2–54,** 347–363.

TenCate, J. A., E. Smith, and R. A. Guyer (2000). Universal slow dynamics in granular solids, *Phys. Rev. Lett.* **85,** 1020–1023.

Wegler, U., and C. Sens-Schonfelder (2007). Fault zone monitoring with passive image interferometry, *Geophys. J. Int.* **168,** no. 3, 1029–1033.

Yamazoe, M., K. Kato, A. Yamada, and M. Takemura (2004). Estimation of *S*-wave velocity at KiK-net Hakuta and Hino stations, and re-evaluation of bedrock motions during the 2000 Tottoriken-seibu earthquake, *J. Jpn. Ass. Earthq.* **4,** 107–125 (in Japanese with English abstract).

## Appendix

### Derivation of the Theoretical Coda Deconvolution

This appendix shows the derivation of the theoretical coda deconvolution. We denote the back azimuth and inci-

dent angle of an incident wave as $\phi$ and $\theta$, respectively (see Fig. 7). We define $\phi = 0$ for the incidence from west to east and $\theta = 0$ for the vertical incidence. The back azimuth increases counterclockwise. The east–west and north–south components of the incident *SH* and *SV* waves are given in the frequency domain by

$$\begin{aligned} A_{SH,\mathrm{EW}}(\theta,\phi,f) &= A_{SH}(\theta,\phi,f)\sin\phi, \\ A_{SV,\mathrm{EW}}(\theta,\phi,f) &= -A_{SV}(\theta,\phi,f)\cos\phi\cos\theta, \\ A_{SH,\mathrm{NS}}(\theta,\phi,f) &= -A_{SH}(\theta,\phi,f)\cos\phi, \\ A_{SV,\mathrm{NS}}(\theta,\phi,f) &= -A_{SV}(\theta,\phi,f)\sin\phi\cos\theta, \end{aligned} \tag{A1}$$

where $A_{SH}(\theta,\phi,f)$ and $A_{SV}(\theta,\phi,f)$ are the complex spectra of the incident *SH* and *SV* waves, respectively. We assume that these incident waves are stationary and the duration of these signals is long enough so that we can assume the ergodic system. We also denote the response functions to horizontal components of the incident *SH* and *SV* waves as $T_{SH}(\theta,f)$ and $T_{SV}(\theta,f)$ on the ground surface and as $R_{SH}(\theta,f)$ and $R_{SV}(\theta,f)$ at the downhole, respectively. From equation (A1) and the response functions, the horizontal component of the spectrum on the ground surface $S(\theta,\phi,f)$ and that at the downhole $B(\theta,\phi,f)$ for each back azimuth and incident angle are given by

$$\begin{aligned} S_X(\theta,\phi,f) &= A_{SH,X}(\theta,\phi,f)T_{SH}(\theta,f) \\ &\quad + A_{SV,X}(\theta,\phi,f)T_{SV}(\theta,f), \\ B_X(\theta,\phi,f) &= A_{SH,X}(\theta,\phi,f)R_{SH}(\theta,f) \\ &\quad + A_{SV,X}(\theta,f)R_{SV}(\theta,f), \end{aligned} \tag{A2}$$

where the subscript $X$ denotes the east–west or north–south component. The wave field is calculated by integrating equation (A2) by $\theta$ and $\phi$. Therefore, the theoretical cross spectrum and power spectrum at the downhole are given by

$$\begin{aligned} \langle S_X^T(f)B_X^{T^*}(f)\rangle &= \left\langle \int_0^{\pi/2}\int_0^{2\pi} S_X(\theta,\phi,f)\sin\theta\,d\phi\,d\theta \right. \\ &\quad \left. \times \int_0^{\pi/2}\int_0^{2\pi} B_X^*(\theta',\phi',f)\sin\theta'\,d\phi'\,d\theta' \right\rangle \end{aligned} \tag{A3}$$

and

$$\begin{aligned} \langle |B_X^T(f)|^2\rangle &= \left\langle \int_0^{\pi/2}\int_0^{2\pi} B_X(\theta,\phi,f)\sin\theta\,d\phi\,d\theta \right. \\ &\quad \left. \times \int_0^{\pi/2}\int_0^{2\pi} B_X^*(\theta',\phi',f)\sin\theta'\,d\phi'\,d\theta' \right\rangle, \end{aligned} \tag{A4}$$

respectively, where the angular brackets indicate the average for the incidence of incoherent waves from any direction. Substituting equation (A2) into equations (A3) and (A4), we obtain

$$\begin{aligned} &\langle S_X^T(f)B_X^{T^*}(f)\rangle \\ &= \left\langle \int_0^{\pi/2}\int_0^{2\pi} A_{SH,X}(\theta,\phi,f)T_{SH}(\theta,f)\sin\theta\,d\phi\,d\theta \right. \\ &\quad \left. \times \int_0^{\pi/2}\int_0^{2\pi} A_{SH,X}^*(\theta',\phi',f)R_{SH}^*(\theta',f)\sin\theta'\,d\phi'\,d\theta' \right\rangle \\ &\quad + \left\langle \int_0^{\pi/2}\int_0^{2\pi} A_{SH,X}(\theta,\phi,f)T_{SH}(\theta,f)\sin\theta\,d\phi\,d\theta \right. \\ &\quad \left. \times \int_0^{\pi/2}\int_0^{2\pi} A_{SV,X}^*(\theta',\phi',f)R_{SV}^*(\theta',f)\sin\theta'\,d\phi'\,d\theta' \right\rangle \\ &\quad + \left\langle \int_0^{\pi/2}\int_0^{2\pi} A_{SV,X}(\theta,\phi,f)T_{SV}(\theta,f)\sin\theta\,d\phi\,d\theta \right. \\ &\quad \left. \times \int_0^{\pi/2}\int_0^{2\pi} A_{SH,X}^*(\theta',\phi',f)R_{SH}^*(\theta',f)\sin\theta'\,d\phi'\,d\theta' \right\rangle \\ &\quad + \left\langle \int_0^{\pi/2}\int_0^{2\pi} A_{SV,X}(\theta,\phi,f)T_{SV}(\theta,f)\sin\theta\,d\phi\,d\theta \right. \\ &\quad \left. \times \int_0^{\pi/2}\int_0^{2\pi} A_{SV,X}^*(\theta',\phi',f)R_{SV}^*(\theta',f)\sin\theta'\,d\phi'\,d\theta' \right\rangle \end{aligned} \tag{A5}$$

and

$$\begin{aligned} &\langle |B_X^T(f)|^2\rangle \\ &= \left\langle \int_0^{\pi/2}\int_0^{2\pi} A_{SH,X}(\theta,\phi,f)R_{SH}(\theta,f)\sin\theta\,d\phi\,d\theta \right. \\ &\quad \left. \times \int_0^{\pi/2}\int_0^{2\pi} A_{SH,X}^*(\theta',\phi',f)R_{SH}^*(\theta',f)\sin\theta'\,d\phi'\,d\theta' \right\rangle \\ &\quad + \left\langle \int_0^{\pi/2}\int_0^{2\pi} A_{SH,X}(\theta,\phi,f)R_{SH}(\theta,f)\sin\theta\,d\phi\,d\theta \right. \\ &\quad \left. \times \int_0^{\pi/2}\int_0^{2\pi} A_{SV,X}^*(\theta',\phi',f)R_{SV}^*(\theta',f)\sin\theta'\,d\phi'\,d\theta' \right\rangle \\ &\quad + \left\langle \int_0^{\pi/2}\int_0^{2\pi} A_{SV,X}(\theta,\phi,f)R_{SV}(\theta,f)\sin\theta\,d\phi\,d\theta \right. \\ &\quad \left. \times \int_0^{\pi/2}\int_0^{2\pi} A_{SH,X}^*(\theta',\phi',f)R_{SH}^*(\theta',f)\sin\theta'\,d\phi'\,d\theta' \right\rangle \\ &\quad + \left\langle \int_0^{\pi/2}\int_0^{2\pi} A_{SV,X}(\theta,\phi,f)R_{SV}(\theta,f)\sin\theta\,d\phi\,d\theta \right. \\ &\quad \left. \times \int_0^{\pi/2}\int_0^{2\pi} A_{SV,X}^*(\theta',\phi',f)R_{SV}^*(\theta',f)\sin\theta'\,d\phi'\,d\theta' \right\rangle. \end{aligned} \tag{A6}$$

We assume that $A_{SH,X}(\theta,\phi,f)$ and $A_{SV,X}(\theta,\phi,f)$ are mutually incoherent for any incident angles. In this case, the second and third terms of the right-hand side of equations (A5) and (A6) disappear by the averaging. Using equation (A1), we can rewrite the north–south component of the equations (A5) and (A6) as

$$\langle S_{NS}^{T}(f)B_{NS}^{T^*}(f)\rangle = \int_0^{\pi/2}\int_0^{\pi/2} T_{SH}(\theta,f)R_{SH}^{*}(\theta',f)\int_0^{2\pi}\int_0^{2\pi}\langle A_{SH}(\theta,\phi,f)A_{SH}^{*}(\theta',\phi',f)\rangle\cos\phi\cos\phi'\sin\theta\sin\theta'\,d\phi'\,d\phi\,d\theta'\,d\theta + \int_0^{\pi/2}\int_0^{\pi/2} T_{SV}(\theta,f)R_{SV}^{*}(\theta',f) \times \int_0^{2\pi}\int_0^{2\pi}\langle A_{SV}(\theta,\phi,f)A_{SV}^{*}(\theta',\phi',f)\rangle\sin\phi\cos\theta\sin\phi'\cos\theta'\sin\theta\sin\theta'\,d\phi'\,d\phi\,d\theta'\,d\theta \quad \text{(A7)}$$

and

$$\langle |B_{NS}^{T}(f)|^2\rangle = \int_0^{\pi/2}\int_0^{\pi/2} R_{SH}(\theta,f)R_{SH}^{*}(\theta',f)\int_0^{2\pi}\int_0^{2\pi}\langle A_{SH}(\theta,\phi,f)A_{SH}^{*}(\theta',\phi',f)\rangle\cos\phi\cos\phi'\sin\theta\sin\theta'\,d\phi'\,d\phi\,d\theta'\,d\theta + \int_0^{\pi/2}\int_0^{\pi/2} R_{SV}(\theta,f)R_{SV}^{*}(\theta',f) \times \int_0^{2\pi}\int_0^{2\pi}\langle A_{SV}(\theta,\phi,f)A_{SV}^{*}(\theta',\phi',f)\rangle\sin\phi\cos\theta\sin\phi'\cos\theta'\sin\theta\sin\theta'\,d\phi'\,d\phi\,d\theta'\,d\theta, \quad \text{(A8)}$$

respectively. Here, we also assume that the incident waves coming from different back azimuths or incident angles are mutually incoherent. In this case, according to the definition of the delta function for the spherical coordinate (e.g., Snieder, 2004), the angular brackets in equations (A7) and (A8) are given by

$$\langle A_{SH}(\theta,\phi,f)A_{SH}^{*}(\theta',\phi',f)\rangle = \langle A_{SV}(\theta,\phi,f)A_{SV}^{*}(\theta',\phi',f)\rangle = \frac{|A(f)|^2}{\sin\theta'}\delta(\theta-\theta')\delta(\phi-\phi'), \quad \text{(A9)}$$

where $|A(f)|^2$ is the average power spectrum of the incident *SH* and *SV* waves. Because we assume that incident *SH* and *SV* waves have statistically the same amplitude for all directions, the average power spectrum does not vary with $\theta$ and $\phi$. Substituting equation (A9) into equations (A7) and (A8) and calculating the integrals for $\theta'$, $\phi'$, and $\phi$, we derive the results as

$$\langle S^{T}(f)B^{T^*}(f)\rangle = \pi|A(f)|^2\int_0^{\pi/2}[T_{SH}(\theta,f)R_{SH}^{*}(\theta,f) + T_{SV}R_{SV}^{*}(\theta,f)\cos^2\theta]\sin\theta\,d\theta \quad \text{(A10)}$$

and

$$\langle |B^{T}(f)|\rangle = \pi|A(f)|^2\int_0^{\pi/2}[|R_{SH}(\theta,f)|^2 + |R_{SV}(\theta,f)|^2\cos^2\theta]\sin\theta\,d\theta. \quad \text{(A11)}$$

We remove the subscripts EW or NS from equations (A10) and (A11) because both components give the same result. Using equations (A10), (A11), and (3), from the main text, we calculate the theoretical coda deconvolution.

Department of Geophysics
Graduate School of Science
Tohoku University
Aramaki-Aza-Aoba 6-3, Aoba-ku
Sendai-shi, Miyagi-ken 980-8578, Japan
sawa@zisin.geophys.tohoku.ac.jp

Manuscript received 6 May 2008